IEEE Access
Multidisciplinary | Rapid Review | Open Access Journal

Received 2 August 2023, accepted 1 September 2023, date of publication 11 September 2023,
date of current version 15 September 2023.

Digital Object Identifier 10.1109/ACCESS.2023.3313777

RESEARCH ARTICLE

A Stability Quantitative Analysis Method of Three-Phase Four-Wire Grid-Connected Systems Considering Frequency Coupling and Sequence Components Coupling

YUMING LIAO, YAOXIN WANG, (Student Member, IEEE), HENG NIAN, (Senior Member, IEEE), HAIPAN LI, YUKUN QIU, AND DAN SUN, (Senior Member, IEEE)
College of Electrical Engineering, Zhejiang University, Hangzhou 310027, China

Corresponding author: Heng Nian (nianheng@zju.edu.cn)

This work was supported by the National Natural Science Foundation of China under Grant 51977194.

ABSTRACT Distribution three-phase four wire power systems are undergoing significant evolutions in physical and technical features as a result of the large-scale integration of rooftop solar photovoltaics. For such multi-converter power systems, the occurred oscillation issues usually involve a variety of components. In addition, the intertwined relationship between dual frequency coupling effect and sequence components coupling effect complicates the analysis processes and makes the existing analysis results not suitable. To analyze the oscillation characteristics accurately of such system, this paper proposes a quantitative analysis method of oscillation mode based on the admittance network model, which considers dual frequency coupling effect, sequence components coupling effect and their intertwined relationship. In addition, a method to calculate the accurate characteristic roots effectively and flexibly based on a partitioned interval ant colony algorithm is also proposed. Finally, the node oscillation participation factor and oscillation mode sensitivity are defined to reveal the oscillation characteristics and laws of the three-phase four-wire grid-connected systems. The time-domain simulations results implemented in MATLAB/Simulink validate the analytical results.

INDEX TERMS Three-phase four wire system, dual frequency coupling effect, impedance, quantitative analysis, oscillation mode.

I. INTRODUCTION

Distribution power systems are undergoing significant evolutions in physical and technical features as a result of the large-scale integration of rooftop solar photovoltaics [1], [2]. Driven by falling prices and improvements in technology, the installation of rooftop solar photovoltaics on distribution grids has increased dramatically in recent years. And the configuration shown in Figure 1 become a common scenario [3], [4], [5], [6], [7], [8] in which single-phase rooftop photovoltaic inverters (SI) are divided into three phase group and connected to the three-phase four-wire distribution grid in star (Y) configuration. Concurrently, three-phase four-wire energy storage inverters (TFESI) are integrated into the system to provide energy support and enhance system damping. The interactions between the weak grid and converters may cause system oscillation [9], [10], [11], [12]. The oscillation

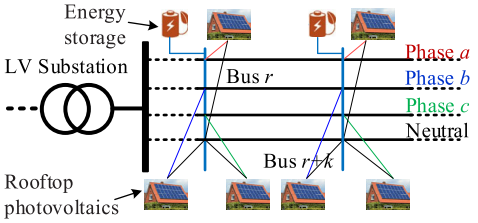

FIGURE 1. Configurations of SIs connected to three-phase four-wire weak grid with TFESI connected.

The associate editor coordinating the review of this manuscript and approving it for publication was Feiqi Deng.

issues in such multi-converter power systems usually involve various components and affect a large area. To monitor and control the oscillations effectively, the oscillatory current distribution and the contribution of each node to the oscillation need to be known. Therefore, it is also important to obtain the oscillation characteristics accurately and identify the origin and weak point of oscillation effectively.

The stability of converters is influenced by several factors. Research have demonstrated that the dynamics of both outer and inner controllers of the converter, in addition to time delay, can result in negative effect to the system stability [13]. Furthermore, for grid-connected converters, recent research has indicated that phase-lock loop (PLL) can cause potential stability issues under weak grid [14], [15], [16].

To the multi-harmonics couplings, [17] presents a harmonic-domain single input single-output (SISO) equivalent modeling technique for the impedance modeling and stability analysis of a single-phase grid connected converter. The proposed SISO modeling concept makes it intuitive to identify the stability of the system. Reference [18] established a 3*3 impedance model to capture the coupling frequency components with improved accuracy. Reference [19] showed that the SOGI based PLL might cause the system instability when the bandwidth of PLL is high or the strength of the grid is weak. The paper also indicated that the frequency feedback control could lead to the nonlinear coupling characteristic between different frequency components. In [20], an impedance considering the frequency coupling effect is established, and the robust PLL by a grid current feedforward is discussed to improve the system stability. Reference [21] establishes an accurate model of the SOGI-PLL and studies the influences of various PLL parameters on the performance of SOGI-PLL based on a complicated graphical method. References [22] and [23] established the impedance models for three-phase four-wire inverters, and evaluated stability of the system in basis on the impedances of the grid and inverter by the generalized Nyquist criterion (GNC). these papers indicate that the zero-sequence component may also lead to system instability and the transmission power of the inverter make a significant difference on the stability of the system. It should be noted that, the stability issues of the system with multiple-inverters connected to multiple-nodes would be more complicated and severer due to the complex interactions between the converters and intricate grid impedances [24].

Many researches have been conducted on the stability analysis of multi-converter power systems, which have been implemented using either state-space models [25], [26] or impedance models [27], [28], [29], [30], [31], [32], [33]. However, when a large number of distributed generations are connected to the system, the state-space model becomes complex and stability assessment becomes time-consuming. A comprehensive approach for investigating the harmonic stability of small-scale inverter-based power systems was presented in [27]. This approach involves identifying unstable modes step by step applying the impedance-based stability criterion. Nevertheless, repeatedly checking the stability of each inverter step by step could not be efficient for large-scale inverter-connected systems. Reference [28] proposed an alternative modal formulation utilizing real symmetrical nodal matrices, which is more simpler and more efficient than the harmonic resonance mode analysis method. References [29] and [30] proposed a kind of stability criteria to analyze the system analysis with many converters paralleled. However, the strategies may not suitable the system that the converters disperse in complicated geographically structure. To value the system stability in these conditions, the impedance-base analysis method would be a much easier method to implement. Reference [31] values the system stability based on the poles real parts of the multi-input multioutput (MIMO) impedance model. However, this method cannot accurately determine the weak points of the system. In the stability analysis of multi-node systems, it is crucial to determine which nodes are primarily associated with the instability. To achieve this purpose, the Bus participation factor was proposed to obtain the converters which contribute to the corresponding oscillation mode. But the paper more suitable the double-bus system. In [32] an eigenvalue decomposition method is proposed to obtain the observability and controllability of oscillatory modes with the impedance network model as the input. This achievement contributes to obtaining oscillatory characteristics of system. Reference [33] established the nodal admittance matrix of the system and the output admittance of the converters to formulate the return-ratio matrix and analyze the system stability. And the location optimization method for multi converter power systems are also proposed.

However, compared with the three-phase three-wire system, an additional zero-sequence path exists in the three-phase four-wire system. Tus, considering only the positive-sequence (PS) and negative-sequence (NS) components does not fully reflect the completely information of the system, as the zero-sequence (ZS) component can also lead to system instability [22]. This makes the existing stability analysis results [25], [26], [27], [28], [29], [30] not fully applicable, as the positive and negative components only considered. Moreover, it should be noted that the incorporation of ZS components in addition to PS and NS components in a three-phase four-wire system renders the existing nodal admittance matrix constructed in previous work inapplicable. And the nodal admittance matrix (NAM) for the three-phase four-wire system is not a simple matter of adding an additional dimension to the existing matrix that considers only positive and NS components. The multi-frequency coupling effect of single-phase inverters and potential asymmetric operating states further complicate the nodal admittance matrix for the system. Specifically, the system may have positive, negative, and ZS components of multiple coupling frequencies simultaneously, which makes the original two-dimensional matrix inadequate in accurately describing the small signal state of the system. Consequently, to accurately describe the small signal loop in the system, it is necessary to establish a higher-dimensional nodal admittance matrix that takes

into account the $f\pm2f_1$ frequency-coupled component and the asymmetric operating state, where f_1 is the fundamental frequency.

In addition, as previously mentioned, the evaluation of system stability is reliant on the roots of the determinant of the nodal admittance matrix [31], [32], [33]. And the determinant is a polynomial of high-order. To solve the roots of the determinant, a partitioned interval ant colony algorithm is proposed by this paper. The proposed method is based on the foraging principle of ant colonies. The minimal value of the determinant of the nodal admittance matrix is set as an objective function in the interval, and the zeros of the determinant can be easily and accurately obtained. The method has the advantages of high computational accuracy, good convergence, and ease of implementation, making it suitable for calculating the zeros of NAM determinant.

In summary, the stability analysis of three-phase four-wire system integrated with large scare single-phase inverters considering the intertwined relationship between dual frequency coupling effect and sequence components coupling characteristic has not received much attention and sufficient investigation. And the reason why this paper didn't consider the control in the system [34], [35], [36], [37] is that the paper aims to reveal the mechanism of small-signal instability in three-phase four-wire systems from an impedance perspective and analyze the influence of different parameters on system stability. The harmonic issues discussed in [36] and [37] are different from the harmonic studied in this paper. Because the harmonics studied in [36] and [37] are caused by loads or grid-connected devices, while the harmonics investigated in this paper are the harmonic components that arise from insufficient system damping leading to system divergence after being subjected by small disturbances. In order to address this issue, the paper establishes the node admittance matrix considering ZS impedance and dual frequency coupling effect (DFCE), and a method for calculating the characteristic roots based on a partitioned interval ant colony algorithm is proposed. The stability of the system is analyzed based on the proposed method. The contributions and main work and of the paper can be summarized as follows.

(1) A 9n-dimensional NAM of the system, which takes into account the dual frequency coupling effect and sequence components coupling effect is constructed to include full information of the system topology and all oscillation modes. This allows for accurate assessment of oscillation stability.

(2) To solve the roots of the determinant of the nodal admittance matrix efficiently, and avoiding the complicated inversion operations of the high dimensional matrix, a partitioned interval ant colony algorithm is proposed to achieve the accurate characteristic roots of the system.

(3) The participation factor of the oscillation mode has been defined to quantify the contribution of each node to the oscillation mode and to locate the weaknesses of the system. Based on the NAM, the relationships between the oscillation and dominant factors are also revealed through the oscillation mode sensitivity, which describes the oscillation behavior of the system.

And the rest of the paper is organized as follows. Impedance modeling of the single-phase rooftop solar photovoltaics and three-phase four wire energy storage inverter are established in Section II. Then, the quantitative stability analysis method based on partitioned interval ant colony algorithm of oscillation mode is proposed in Section III. Section IV analyzes the oscillation characteristic and mechanism of the system. The time-domain simulations are also implemented for verification in Section IV. Finally, Section V shows a summary of the conclusions.

II. IMPEDANCE MODELLINGS OF THE SINGLE-PHASE ROOFTOP SOLAR PHOTOVOLTAICS AND THREE-PHASE FOUR WIRE ENERGY STORAGE INVERTER

This section shows the topology structure of the investigated system and establishes the impedance models of the SI, TFESI transmission line and ac grid, considering the intertwined relationship between dual frequency coupling effect and sequence components coupling effect.

A. SYSTEM TOPOLOGY STRUCTURE

The main objective of this research is to investigate the stability and oscillation mode in multi-node systems within three-phase four-wire distribution networks, and to examine the effects of critical parameters on overall system stability. In order to ensure a comprehensive analysis, the topology presented in Figure 2 has been employed, which includes SIs, TFESIs, transmission line, AC grid.

This is a common scenario in distribution networks of the townships connected with large scale distribution source [8], wherein numerous single-phase photovoltaic systems are connected to the three-phase four-wire distribution grid. The system consists of a total of n nodes, with m_k^*3 single-phase photovoltaic inverters connected at each node. These m_k^*3 single-phase photovoltaic inverters are distributed across the three phases. In relation to node k, three-phase four-wire energy storage inverters are also connected to bolster the system's energy support. To ensure the applicability of the research, the placement of energy storage systems can be determined based on the importance and requirements of the users. The $L_{k-1,k}$ and $R_{Lk-1,k}$ are the inductance and resistance of transmission lines between node k-1 and node k.

During the development of the node admittance matrix, it is insufficient to simply add an extra dimension based on the conventional node admittance matrix. Instead, it is crucial to consider the interactions among PS, NS, and ZS, in addition to the simultaneous presence of multi-frequency harmonic components. Such an approach may result in suboptimal analytical precision when employing the node admittance matrix directly from the referenced literature [31], [32], [33].

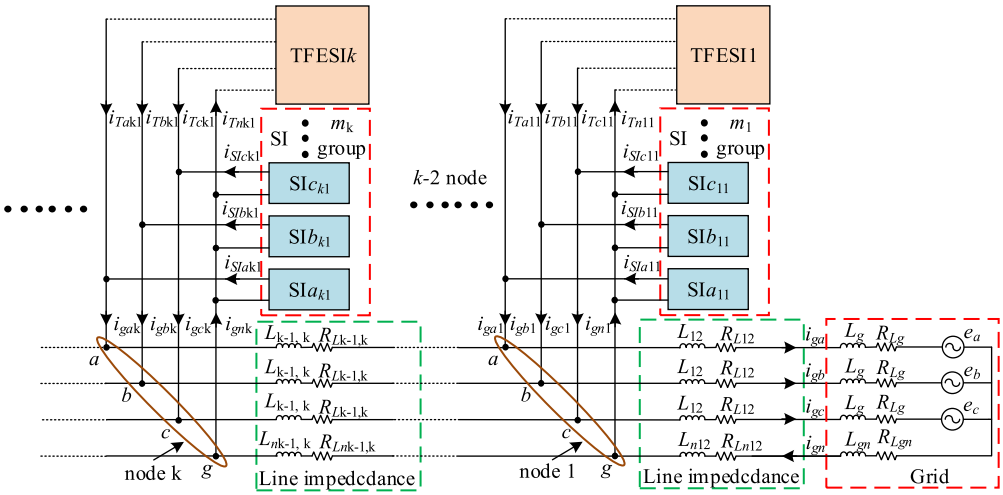

FIGURE 2. Schematic diagram of the invested system.

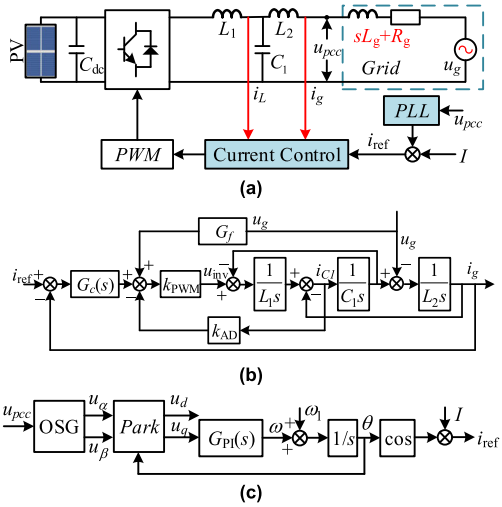

FIGURE 3. Schematic and control strategy of the SI. (a) Schematic of the SI connected to the weak grid. (b) Control block of the current controller. (c) Control block of the PLL.

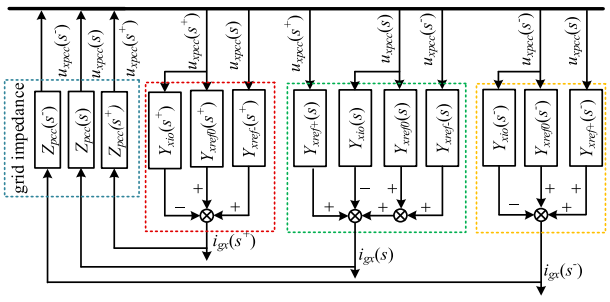

FIGURE 4. Voltage and current small signal path diagram of SI.

B. IMPEDANCE MODELING OF SI

Figure 3 shows the schematic and control strategy of the SI. The classical current control strategy of the inverter depicted as Figure 3(b) is applied in this paper. In Figure 3(b), Gf is the PCC voltage feedforward gain, which is selected as 0.6 [41], [42] to improve the robustness of the system. kc is the capacitor current feedforward gain. G_d is the control delay, where $G_d = e^{-1.5Ts}$. T_s is the control period. And Gc is the proportional-resonant (PR) regulator.

The impedance model of SI is presented as shown in equation (1). Figure 4 shows the voltage and current small-signal path figures of the SI, from which it can be seen that in addition to the current and voltage components with a perturbation frequency ω there are also voltage and current components with frequency $\omega \pm 2j\omega_1$ in the system due to the DFCE. The $\omega_1 = 2\pi f_1, f_1 = 50$Hz, it is the rated frequency of the grid. In Figure 4, s represents the Laplace operator. s^- represents negative coupled frequency $s-2j\omega_1$. And s^+ represent the positive coupled frequency $s + 2j\omega_1$.

$$\begin{bmatrix} i_{gx}(s^-) \\ i_{gx}(s) \\ i_{gx}(s^+) \end{bmatrix} = (\mathbf{Y_{xref}}(s) + \mathbf{Y_{xinvo}}(s)) \begin{bmatrix} u_{xpcc}(s^-) \\ u_{xpcc}(s) \\ u_{xpcc}(s^+) \end{bmatrix} \quad (1)$$

where, $\mathbf{Y_{xinvo}}(s) = [Y_{xio}(s^-), 0, 0; 0\ Y_{xio}(s), 0; 0, 0\ Y_{xio}(s^+)]$ and $\mathbf{Y_{xref}}(s)$ can be obtained as (2).

From Figure 4, the grid current i_g at frequencies ω-$2j\omega_1$, ω, and $\omega + 2j\omega_1$ can be seen as (1).

$$\mathbf{Y_{xref}}(s) = \begin{bmatrix} Y_{xref0}(s^-) & Y_{xref+}(s^-) & 0 \\ Y_{xref-}(s) & Y_{xref0}(s) & Y_{xref+}(s) \\ 0 & Y_{xref-}(s^+) & Y_{xref0}(s^+) \end{bmatrix} \quad (2)$$

$Y_{xref-}(s)$, $Y_{xref0}(s)$, and $Y_{xref+}(s)$ represent the transfer relationship from voltage u_{pcc} at frequency $\omega + 2j\omega_1$, ω and ω-$2j\omega_1$ to current i_g at frequency ω respectively. And the definitions of responding mathematical expressions can be expressed as (A1)-(A9) in section Appendix.

Subscript "x" denotes the variables in phase-a, phase-b or phase-c. ϕ_{vx} in (A1)-(A9) denotes the initial phase of the grid. The $G_{OSG\alpha}$ and $G_{OSG\beta}$ denotes the transfer function from

u_{PCC} to u_α and u_β respectively. Without loss of the generality, the time delay based PLL [12], [43] is also applied in the paper, which can be expressed as (3). $T_0 = 0.02$ s, it is the period of the grid voltage.

$$\begin{cases} u_\alpha(s) = G_{osg\alpha}(s)\, u_{pcc}(s) = u_{pcc}(s) \\ u_\beta(s) = G_{osg\beta}(s)\, u_{pcc}(s) = u_{pcc}(s)\, e^{-T_0 s/4} \end{cases} \tag{3}$$

Due to the proximity to each other, the inverters in different groups of the same phase can be considered to be in parallel with each other. Assuming that node i has $3{*}m_i$ single-phase inverters, the admittance expression of the inverters in group j of the i-th node can be shown in (4). In equation (4), x = a,b,c denotes phase-a, phase-b and phase-c.

$$\begin{bmatrix} i_{gijx}(s^-) \\ i_{gijx}(s) \\ i_{gijx}(s^+) \end{bmatrix} = \left(\mathbf{Y_{refijx}}(s) + \mathbf{Y_{invoijx}}(s)\right) \begin{bmatrix} u_{pccijx}(s^-) \\ u_{pccijx}(s) \\ u_{pccijx}(s^+) \end{bmatrix} \tag{4}$$

From Figure 1, the currents $i_{giTx}(s^+)$, $i_{giTx}(s)$ and $i_{giTx}(s^-)$ of i-th node produced by SIs can be expressed as,

$$\begin{bmatrix} i_{giTa}(s^-) \\ i_{giTa}(s) \\ i_{giTa}(s^+) \end{bmatrix} = \sum_{j=1}^{mi} \left(\mathbf{Y}_{refija}(s) + \mathbf{Y}_{invoija}(s)\right) \begin{bmatrix} u_{pccia}(s^-) \\ u_{pccia}(s) \\ u_{pccia}(s^+) \end{bmatrix} \tag{5}$$

$$\begin{bmatrix} i_{giTb}(s^-) \\ i_{giTb}(s) \\ i_{giTb}(s^+) \end{bmatrix} = \sum_{j=1}^{mi} \left(\mathbf{Y}_{refijb}(s) + \mathbf{Y}_{invoijb}(s)\right) \begin{bmatrix} u_{pccib}(s^-) \\ u_{pccib}(s) \\ u_{pccib}(s^+) \end{bmatrix} \tag{6}$$

$$\begin{bmatrix} i_{giTc}(s^-) \\ i_{giTc}(s) \\ i_{giTc}(s^+) \end{bmatrix} = \sum_{j=1}^{mi} \left(\mathbf{Y}_{refijc}(s) + \mathbf{Y}_{invoijc}(s)\right) \begin{bmatrix} u_{pccic}(s^-) \\ u_{pccic}(s) \\ u_{pccic}(s^+) \end{bmatrix} \tag{7}$$

By extracting and reintegrating the terms of (5)-(7) for the same frequencies individually, the relationship between the current response and the disturbance voltage at frequencies s^-, s, and s^+ can be obtained as shown in (A10), (A13) and (A17).

By operating the phase-domain to sequence-domain transformation to (A10), (A13) and (A17), the relationship between the current response and the disturbance voltage at frequencies s^-, s, and s^+ can be obtained as shown in equations (A21), (A22) and (A23).

Then combining(A21), (A22) and (A23), the impedance model of node-i SIs considering DFCE can be obtained as a 9×9 admittance, which can be expressed as (8). And the detailed derivation process is shown in Appendix A.

$$\mathbf{I}_{SIi} = \begin{bmatrix} \mathbf{Y}^{012}_{re0i}(s^-) & \mathbf{Y}^{012}_{re+i}(s^-) & 0 \\ \mathbf{Y}^{012}_{re-i}(s) & \mathbf{Y}^{012}_{re0i}(s) & \mathbf{Y}^{012}_{re+i}(s) \\ 0 & \mathbf{Y}^{012}_{re-i}(s^+) & \mathbf{Y}^{012}_{re0i}(s^+) \end{bmatrix} \mathbf{U}_{pcci} \tag{8}$$

In (8), define $\mathbf{I}_{STi} = [i_{gT0}(s^-), i_{gT1}(s^-), i_{gT2}(s^-), i_{gT0}(s), i_{gT1}(s), i_{gT2}(s)\ i_{gT0}(s^+), i_{gT0}(s^+), i_{gT0}(s^+)]$, $\mathbf{U}_{pcci} = [u_{pcci0}(s^-), u_{pcci1}(s^-), u_{pcci2}(s^-), u_{pcci0}(s), u_{pcci1}(s), u_{pcci2}(s), u_{pcci0}(s^+), u_{pcci1}(s^+), u_{pcci2}(s^+)]$.

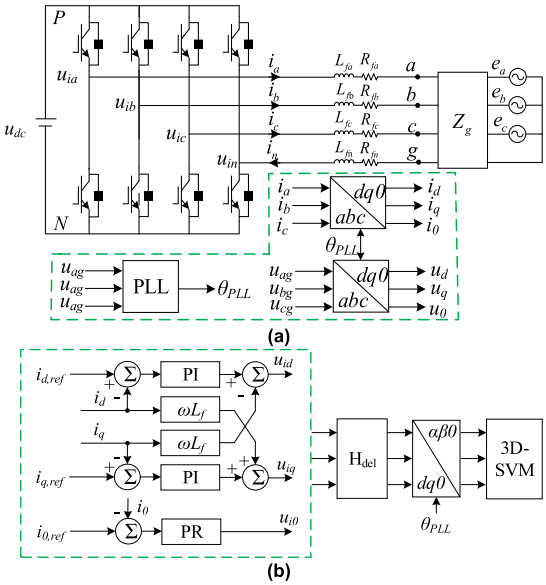

FIGURE 5. Schematic and control strategy of the TFESI. (a) Schematic of the TFESI connected to the grid. (b) Control block of the TFESI.

The (8) establishes a mathematical model for describing the correlation between the response of disturbance voltage and current in a single-phase photovoltaic inverter system. The incomplete uniformity in output power among different photovoltaic inverters causes the system to exhibit simultaneous positive, negative, and ZS components with frequencies of s^-, s, and s^+, correspondingly.

And the above expression can be denoted as,

$$\mathbf{I}_{SIi} = \mathbf{Y}_{SIT}\mathbf{U}_{pcci} \tag{9}$$

C. IMPEDANCE MODELING OF TFESI

Figure 5 shows the schematic and control strategy of the TFESI. The TFESI are integrated into the system to provide energy support and enhance system damping. The control block diagram of the system includes the PLL, and the control delay, the current PI controller and 3D-SVM modulation module [44].

And the impedance of the TFGI can be expressed as [22],

$$\mathbf{Y_{i0pn}} = \mathrm{T}_Z \mathbf{Y}_{0dq} \mathrm{T}_Z^{-1} = \begin{bmatrix} \mathbf{Y_{i0}} & \mathbf{0} \\ \mathbf{0} & \mathbf{Y_{ipn}} \end{bmatrix} = \begin{bmatrix} Y_{00} & 0 & 0 \\ 0 & Y_{11} & Y_{12} \\ 0 & Y_{21} & Y_{22} \end{bmatrix} \tag{10}$$

In (10), the Y_{00} is the ZS admittance, Y_{11} is the PS admittance, Y_{22} is the NS admittance. And the Y_{12} and Y_{21} are the coupling admittances between PS admittance and NS admittance. It should be noted that the elements in third column or third row in matrix $\mathbf{Y_{ipn0}}$ except the third element in the third column elements are zero, which means the relationship between positive-sequence admittance and zero-sequence admittance is decoupled, and the relationship

between negative -sequence admittance and zero-sequence admittance is also decoupled.

The coexistence of positive, negative, and ZS voltage disturbance components with frequencies of s^-, s, and s^+ in the power system poses a significant challenge to power system stability analysis. According to (10), it can be seen that a PS voltage at frequency s generates a NS current at frequency s^-, so a NS voltage at frequency s will also generates a PS current of frequency s^+ by the recursive operation. This makes (10) impossible to accurately describe the relationship between the disturbance voltage and the disturbance current response.

To address this issue, it is essential to expand the admittance matrix, shown as (10), that considers only the NS component with a frequency of s^- and the PS as well as ZS components with a frequency of s. This expansion enables the recursive operation on frequency, which establishes the relationship between the voltage disturbance and current response components with PS, NS, and ZS with frequencies of s^-, s, and s^+. The expanded admittance matrix can be represented by (11), as shown at the bottom of the next page.

And the (11) can be denoted as,

$$\mathbf{I}_{TFGIi} = \mathbf{Y}_{TFGI}\mathbf{U}_{pcci} \tag{12}$$

D. IMPEDANCE MODELE OF TRANSMISSION LINE AND GRID

Transmission lines can be represented by either T-model or π-model equivalent circuits [45]. As the capacitance effect of the transmission line possesses negligible effect on the system dynamics [46], the admittance model of the transmission line between node i and node j can be expressed as (13), shown at the bottom of the next page.

In (13),$Y_{0Lij} = 1/(sL_{ij}+R_{ij}+3(sL_{nij}+R_{nij}))$, $Y_{1Lij} = Y_{2Lij} = 1/(sL_{ij}+ R_{ij})$. L_{ij}, L_{nij}, R_{ij} and R_{nij} are the line inductance and line resistance between node i and node j. And s^- represents negative coupled frequency $s-2j\omega_1$. And s^+ represent the positive coupled frequency $s + 2j\omega_1$.

Similarly, the impedance of the AC grid can be obtained as (14), shown at the bottom of the next page. In equation (14), the $Y_{0g} = 1/(sL_g + R_g+3(sL_{gn} + R_{gn}))$, $Y_{1g} = Y_{2g} = 1/(sL_g + R_g)$, L_g, L_{gn}, R_g, R_{gn} are the equivalent grid inductance and equivalent grid resistance of the transformers and transmission lines.

III. QUANTITATIVE ANALYSIS METHOD OF THE OSCILLATION MODE

As shown in Figure 1, the oscillation characteristics of the system are influenced by the interactions among all SIs, TFESIs, transmission lines and AC grid.

Reference [22] points out that the presence of ZS path in the three-phase four-wire system necessitates the consideration of ZS components when assessing system stability. Furthermore, the frequency coupling characteristics of single-phase inverters differ from conventional three-phase three-wire inverters, as they exhibit two frequency coupling components with frequencies of s-$2j\omega_1$ and $s + 2j\omega_1$, respectively. Existing oscillation analysis methods have not incorporated the multi-frequency coupling and ZS components of single-phase inverters. As a result of this limitation, the accurate analysis of the oscillation characteristics and laws of the system is impeded.

Therefore, this section proposes a quantitative analysis method of oscillation mode which considers the intertwined relationship between dual frequency coupling effect and sequence components coupling effect based on the NAM.

A. OSCILLATION MODE OF THE SYSTEM

The system depicted in Figure 1 comprises of n nodes. The current-voltage relationship of the system, accounting for ZS components and frequency coupling characteristics, can be represented by the nodal admittance matrix, as depicted in equation (15), as shown at the bottom of the next page. The NAM is denoted as $\mathbf{Y}_{SN}(s)$, which is a 9n × 9n matrix. n is the number of nodes. The node current vector matrix I(s) and node voltage vector matrix U(s) are expressed as $\mathbf{I}_i = [I_{pi}(s^-), I_{ni}(s^-), I_{zi}(s^-), I_{pi}(s), I_{ni}(s), I_{zi}(s), I_{pi}(s^+), I_{ni}(s^+), I_{zi}(s^+)]^T$, $\mathbf{U}_i = [U_{pi}(s^-), U_{ni}(s^-), U_{zi}(s^-), U_{pi}(s), U_{ni}(s), U_{zi}(s), U_{pi}(s^+), U_{ni}(s^+), U_{zi}(s^+)]^T$, $i = 1,\ldots,n$.

According to (15), the transfer function of the system can be obtained as (16). And the system oscillation modes can be identified by finding the zeros of $\det[\mathbf{Y}_{SN}(s)]$ shown as (17).

$$\mathbf{U}(s) = \mathbf{Y}_{SN}(s)^{-1}\mathbf{I}(s) = \frac{\mathbf{Y}_{SN}(s)^*}{\det[\mathbf{Y}_{SN}(s)]}\mathbf{I}(s) \tag{16}$$

$$\det[\mathbf{Y}_{SN}(s_k)] = 0 \tag{17}$$

The oscillation modes occur in group of three frequency components due to the DFCE of single-phase inverters and ZS components being accounted for. The k-th oscillation modes, denoted as s_k, which can be defined as $s_{k,1} = -\sigma_k + j2\pi f_{k,1}$, $s_{k,2} = -\sigma_k + j2\pi f_{k,2}$ and $s_{k,3} = -\sigma_k + j2\pi f_{k,3}$. In this context, σ_k denotes the damping of the oscillation modes. The oscillation frequencies of the same group oscillation modes are represented by $f_{k,1}$, $f_{k,2}$ and $f_{k,3}$, and they satisfy the relationship $f_{k,2} = 2f_1 + f_{k,1}$, $f_{k,3} = 2f_1 + f_{k,2}$. It can be seen that the three parts have the same damping and the frequencies differ from $2f_1$. When the real parts of all oscillation modes are negative, the system can maintain stale.

B. PARTICIPATION FACTOR

The node oscillation participation factor is then derived from the oscillation modes. The complex constant matrix $\mathbf{Y}_{SN}(s_k)$ is obtained by substituting the oscillation mode s_k into (15). Based on the eigenvalue decomposition theory [47], $\mathbf{Y}_{SN}(s_k)$ is diagonalized as shown in (18).

$$\mathbf{Y}_{SN}(s_k) = \mathbf{R}_\Lambda \times \Lambda \times \mathbf{L}_\Lambda^T \tag{18}$$

In (18), the matrix of eigenvalues can be obtained as $\Lambda = \mathrm{diag}(\lambda_1, \lambda_2,\ldots, \lambda_{9n})$; the right and left eigenvector matrices are $\mathbf{R}_\Lambda = [\mathbf{R}_{\Lambda 1}, \mathbf{R}_{\Lambda 2},\ldots, \mathbf{R}_{\Lambda 9n}]$ and $\mathbf{L}_\Lambda = [\mathbf{L}T\ \Lambda 1, \mathbf{L}T\ \Lambda 2,\ldots, \mathbf{L}T\ \Lambda 9n]$, respectively; the $\mathbf{R}_\Lambda$ and $\mathbf{L}_\Lambda$ satisfy $\mathbf{R}$-1 $\Lambda = \mathbf{L}T\ \Lambda$.

A zero eigenvalue (denoted as λ_{sk}) for $\mathbf{Y}_{SN}(s_k)$ exists because its determinant is zero. Equation (19) can be obtained by substituting (18) into (15).

$$\mathbf{L}_{\Lambda}^{T}\mathbf{U}(s_k) = \Lambda^{-1}\mathbf{L}_{\Lambda}^{T}\mathbf{I}(s_k) \tag{19}$$

From (19), the mode voltage $\mathbf{V}(s)$ and the mode current $\mathbf{J}(s)$ are defined as $\mathbf{V}(s) = \mathbf{L}\mathrm{T}\ \Lambda\mathbf{U}(s)$ and $\mathbf{J}(s) = \mathbf{L}\mathrm{T}\ \Lambda\mathbf{I}(s)$, respectively. The mode voltage and the mode current corresponding to λ_{sk} have the relationship given by (20).

$$V_{sk} = \lambda_{sk}^{-1}J_{sk} \tag{20}$$

Because of $\lambda_{sk} = 0$, the mode current J_{sk} induces a large mode voltage V_{sk} at this point, and this mode voltage dominates the voltage at each node of the system. Equation (21) shows the algebraic function of the node voltage and node current.

$$\begin{aligned}\mathbf{U}(s_k) &= \mathbf{R}_{\Lambda}\mathbf{V}(s_k) \approx \mathbf{R}_{\Lambda sk}V_{sk} = \mathbf{R}_{\Lambda sk}\lambda_{sk}^{-1}J_{sk} \\ &= \lambda_{sk}^{-1}\mathbf{R}_{\Lambda sk}\mathbf{L}_{\Lambda sk}\mathbf{I}(s_k) = \lambda_{sk}^{-1}\mathbf{P}_{\Lambda sk}\mathbf{I}(s_k)\end{aligned} \tag{21}$$

In (21), $\mathbf{L}_{\mathbf{\Lambda}sk}$ and $\mathbf{R}_{\mathbf{\Lambda}sk}$ are the left and right eigenvectors of λ_{sk}; the diagonal elements of $\mathbf{P}_{\mathbf{\Lambda}sk}$ indicate the participation degree and influence of each node in and by the oscillation mode s_k, respectively.

And the participation factor of node i can be obtained as (22).

$$P_i = \frac{\sum_{h=0}^{8}|P_{sk(9i-h)(9i-h)}|}{\sum_{h=1}^{9n}|P_{skhh}|} \tag{22}$$

where P_{skjj} is the j-th row and j-th column element of $\mathbf{P}_{\mathbf{\Lambda}sk}$.

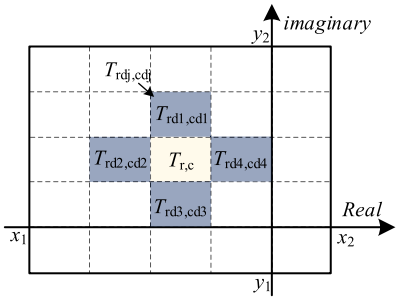

FIGURE 6. Ant colony probable moving path diagram.

C. A METHOD FOR COMPUTING DETERMINANT ZEROS BASED ON INTERVAL-BASED ANT COLONY ALGORITHM

As previously mentioned, the evaluation of system stability is reliant on the roots of the determinant of the nodal admittance matrix, which correspond to the solution of equation (9). Moreover, (9) is a polynomial of high-order. The existing calculation methods rely on the inversion of large matrices and the performance of multiple mathematical operations. When there is a significant number of nodes or when the admittance matrix dimensions of devices connected to the nodes are high (such as the 9-dimensional matrix used in this study), the size of the nodal admittance matrix for the entire system becomes unwieldy, resulting in challenges in solving the zeros of the determinant or the problem of dimensionality disaster. To address these challenges, this paper proposes an interval-based ant colony algorithm to compute the zeros of equation (17).

The computation of the zeros of equation (17) can be reformulated as an optimization problem of determining the minimal value of the function described by equation (17)

$$\begin{bmatrix} i_{giT0}(s^-) \\ i_{giT1}(s^-) \\ i_{giT2}(s^-) \\ i_{giT0}(s) \\ i_{giT1}(s) \\ i_{giT2}(s) \\ i_{giT0}(s^+) \\ i_{giT1}(s^+) \\ i_{giT2}(s^+) \end{bmatrix} = \begin{bmatrix} Y_{00}(s^-) & 0 & 0 & 0 & 0 & 0 & 0 & 0 & 0 \\ 0 & Y_{11}(s^-) & 0 & 0 & 0 & 0 & 0 & 0 & 0 \\ 0 & 0 & Y_{22}(s) & 0 & Y_{21}(s) & 0 & 0 & 0 & 0 \\ 0 & 0 & 0 & Y_{00}(s) & 0 & 0 & 0 & 0 & 0 \\ 0 & 0 & Y_{12}(s) & 0 & Y_{11}(s) & 0 & 0 & 0 & 0 \\ 0 & 0 & 0 & 0 & 0 & Y_{22}(s^+) & 0 & Y_{21}(s^+) & 0 \\ 0 & 0 & 0 & 0 & 0 & 0 & Y_{00}(s^+) & 0 & 0 \\ 0 & 0 & 0 & 0 & 0 & Y_{12}(s^+) & 0 & Y_{11}(s^+) & 0 \\ 0 & 0 & 0 & 0 & 0 & 0 & 0 & 0 & Y_{22}(s^{2+}) \end{bmatrix} \begin{bmatrix} u_{pcci0}(s^-) \\ u_{pcci1}(s^-) \\ u_{pcci2}(s^-) \\ u_{pcci0}(s) \\ u_{pcci1}(s) \\ u_{pcci2}(s) \\ u_{pcci0}(s^+) \\ u_{pcci1}(s^+) \\ u_{pcci2}(s^+) \end{bmatrix} \tag{11}$$

$$\mathbf{Y}_{\mathrm{Lij}} = diag\left(Y_{0Lij}(s^-), Y_{1Lij}(s^-), Y_{2Lij}(s^-), Y_{0Lij}(s), Y_{1Lij}(s), Y_{2Lij}(s), Y_{0Lij}(s^+), Y_{1Lij}(s^+), Y_{2Lij}(s^+)\right) \tag{13}$$

$$\mathbf{Y}_{\mathrm{gij}} = diag\left(Y_{0g}(s^-), Y_{1g}(s^-), Y_{2g}(s^-), Y_{0g}(s), Y_{1g}(s), Y_{2g}(s), Y_{0g}(s^+), Y_{1g}(s^+), Y_{2g}(s^+)\right) \tag{14}$$

$$\begin{bmatrix} \mathbf{I}_1 \\ \mathbf{I}_2 \\ \vdots \\ \mathbf{I}_{n-1} \\ \mathbf{I}_n \end{bmatrix} = \begin{bmatrix} \mathbf{Y}_{SIT1} + \mathbf{Y}_{TFGI1} + \mathbf{Y}_{g1e} + \mathbf{Y}_{g12} & -\mathbf{Y}_{g12} & \cdots & 0 & 0 \\ -\mathbf{Y}_{g12} & \mathbf{Y}_{SIT2} + \mathbf{Y}_{TFGI2} + \mathbf{Y}_{g12} + \mathbf{Y}_{g23} & \cdots & 0 & 0 \\ & & & & \\ 0 & -\mathbf{Y}_{g23} & \vdots & -\mathbf{Y}_{g(n-2,n-1)} & 0 \\ 0 & 0 & \cdots & \mathbf{Y}_{SIT(n-1)} + \mathbf{Y}_{TFGI(n-1)} + \mathbf{Y}_{g(n-2,n-1)} + \mathbf{Y}_{g(n-1,n)} & -\mathbf{Y}_{g(n-1,n)} \\ 0 & 0 & \cdots & -\mathbf{Y}_{gn-1n} & \mathbf{Y}_{SITn} + \mathbf{Y}_{TFGIn} + \mathbf{Y}_{g(n-1,n)} \end{bmatrix} \begin{bmatrix} \mathbf{U}_1 \\ \mathbf{U}_2 \\ \vdots \\ \mathbf{U}_{n-1} \\ \mathbf{U}_n \end{bmatrix} \tag{15}$$

under the constraint that it is equal to zero.

$$f = |\det[\mathbf{Y}_{\mathrm{SN}}(s)]| \tag{23}$$

The function f is the absolute value of the determinant of the nodal admittance matrix as a function of s. Here, s is a complex number with real part a and imaginary part b, where a $\in[x_1, x_2]$ and b$\in[y_1, y_2]$.

For convenience, the interval $[x1, x2]$ can be divided into h_{c} equal-length subintervals and the interval $[y_1, y_2]$ can be divided into h_{r} equal-length subintervals. Consequently, the entire interval is divided into $h_{\mathrm{c}} * h_r$ subintervals. These subintervals are denoted as $\mathrm{T_{r,c}}$, where $\mathrm{T_{r,c}}$ represents the subinterval in the r-th row and c-th column. The midpoint of the interval $\mathrm{T_{r,c}}$ is denoted as a_{rc}+jb_{rc}. The minimal zero points of function f are located within these subintervals.

As illustrated in Figure 6, four adjacent intervals surround interval $\mathrm{T_{r,c}}$. Assuming an ant is present in interval $\mathrm{T_{r,c}}$, its movement path is determined by comparing the function values $f(\mathrm{T_{r,c}})$ of interval $\mathrm{T_{r,c}}$ and function values of its neighboring intervals. If the function value of the ant's current interval is smaller than that of the surrounding intervals, the ant remains stationary, indicating a potential minimum value point in the interval. If the function value of the ant's current interval is larger than the neighboring intervals, the ant must move to an adjacent interval. When multiple neighboring intervals have function values smaller than the current interval, the probability of moving to the corresponding interval is proportional to the difference in function values, with a larger difference resulting in a higher probability. Additionally, the probability of moving to the corresponding interval is also influenced by the pheromone level in the destination interval. If the interval presents more pheromones, there will also be higher probability moving to this interval.

The probability of moving to the corresponding interval can be defined as

$$p_j = \begin{cases} \dfrac{\tau(j)\eta_{ij}}{\sum \tau(h)\eta_{ih}} & , h \in \mathbf{A}_k \\ 0, \ h \notin \mathbf{A}_k \end{cases} \tag{24}$$

where, $\mathbf{A}_k$ denotes the set of subintervals that the ant can move from interval $\mathrm{T_{r,c}}$ to the surrounding intervals. Definition $\eta_{\mathrm{j}} = |f(a_{\mathrm{rc}}, b_{\mathrm{rc}})\text{-}f(a_{\mathrm{rcdj}}, b_{\mathrm{rcdj}})|$, which denotes the difference in function values $f$between interval $\mathrm{T_{r,c}}$ and its surround interval $\mathrm{T_{rdj,cdj}}$. τ(j) represents the pheromones of the surround interval $\mathrm{T_{rdj,cdj}}$. The pheromones indicate the frequency at which ants pass through the interval. For instance, after an ant moves from interval $\mathrm{T_{r,c}}$ to interval $\mathrm{T_{rd2,cd2}}$, the pheromone level in interval $\mathrm{T_{rd2,cd2}}$ increases.

If ant a_{p} has moved from interval $\mathrm{T_{r,c}}$ to interval $\mathrm{T_{rdj,cdj}}$ based on probability, then ant a_{k} leaves pheromones in interval $\mathrm{T_{rdj,cdj}}$. The amount of pheromones left is denoted by $\Delta\tau$(j), Then the $\Delta\tau$ (j) can be expressed as,

$$\Delta\tau_p(j) = C(f(T_{r,c}) - f(T_{rdj,cdj}) \tag{25}$$

In (25), the C is the pheromone increment coefficient, which is set to 1 in this paper.

All ants that move to the interval $\mathrm{T_{rdj,cdj}}$ will leave the corresponding pheromone. Suppose that q ants move to the interval $\mathrm{T_{rdj,cdj}}$. And the total sum of their pheromones left in the interval $\mathrm{T_{rdj,cdj}}$ can be expressed as,

$$\tau(j) = \sum_{p=1}^{q} \Delta\tau_p(j) \tag{26}$$

After numerous moving, some intervals contain a large number of ants, while others have none or few. The intervals with ants are precisely those containing the extreme points, while the intervals without ants are unlikely to contain such points.

Extract the intervals containing ants and refine them further. Repeat the search process until the refined intervals meet the expected accuracy requirements. In the end, all ants will be situated near the extreme points, and the midpoint of the intervals where the ants reside is considered the location of these extreme points. Since oscillation modes appear in groups of three parts, among the identified extreme points, those with an imaginary part differing by 100Hz are considered the system's oscillation modes.

The specific implementation steps of the algorithm defined in this paper are as follows:

Step1: Initialization. The interval $[x_1, x_2]$ can be divided into h_{c} equal-length subintervals and the interval $[y_1, y_2]$ can be divided into h_r equal-length subintervals. And the zone decided by $[x_1, x_2]$ and $[y_1, y_2]$ can be divided into $h_{\mathrm{c}} \times h_{\mathrm{r}}$ equal-area interval. The initial number of ants in the each rectangular interval $T_{\mathrm{r,c}}$ is 1. And the iteration threshold can be defined as ε, which determines the end of the algorithm run process. When the length of the interval is less than the iteration threshold, the system stops the optimization search and outputs the result. Initialize the total number of pheromones $\tau_{\mathrm{r,c}}$ and pheromone increments $\Delta\tau_{\mathrm{r,c}}$, which are set to zero.

Step2: While($\delta > \varepsilon$)

{

Step2.1: All ants move between neighborhoods according to equation (24).

Step2.2: Update the pheromone according to equations (25) and (26).

Step2.3: Update the search range of the colony when all ants no longer perform neighborhood moves, i.e. refine only the intervals where the colony finally gathers (let the number of refinement intervals be $h_{\mathrm{cr}} \times h_{\mathrm{rr}}$). Calculate the length of the refined interval and assign it to δ.

}

Step3:Output the results. The final interval where the ants gather is referred to as the possible interval containing the zeros of equation (17). Additionally, the intervals that possess same real parts and imaginary parts differing by 100Hz are regarded as the intervals that possesses system's oscillation modes. The midpoint of these intervals can be identified as the location of zeros of equation (17).

Based on the aforementioned analysis, it can be deduced that the system will exhibit multiple local minima. Among

TABLE 1. Oscillation modes in Case1.

Oscillation mode	Band-d	Band-m	Band-u
1	-0.5 +j29.60×2π	-0.5 +j70.40×2π	-0.5 +j170.40×2π
2	-5.62 +j48.49×2π	-5.62 +j51.51×2π	-5.62 +j151.51×2π
3	-38.09 +j49.26×2π	-38.09 +j50.74×2π	-38.09 +j150.74×2π

TABLE 2. Oscillation modes in Case2.

Oscillation mode	Band-d	Band-m	Band-u
1	1 +j29.60×2π	1 +j70.40×2π	1 +j170.40×2π
2	-5.60 +j48.49×2π	-5.60 +j51.51×2π	-5.60 +j151.51×2π
3	-38.09 +j49.26×2π	-38.09 +j50.74×2π	-38.09 +j150.74×2π

TABLE 3. Oscillation modes in Case3.

Oscillation mode	Band-d	Band-m	Band-u
1	-2.2 +j29.60×2π	-2.2 +j70.40×2π	-2.2 +j170.40×2π
2	-5.60 +j48.49×2π	-5.60 +j51.51×2π	-5.60 +j151.51×2π
3	-38.09 +j49.26×2π	-38.09 +j50.74×2π	-38.09 +j150.74×2π

these minima, only those with identical real parts and a difference of 100Hz in their imaginary parts, arranged in sets of three, correspond to the characteristic roots of the system. This distinctive characteristic of oscillatory modes contributes to the precision of the computed system characteristic roots. It is highly unlikely to erroneously compute the real and imaginary parts of the three components comprising the same oscillatory mode. The computational accuracy can be further guaranteed by narrowing interval and calculating multiple times. And the advantages of the proposed method can be seen as follow: (1) Only the objective function value at the midpoint of the interval is required, avoiding the complex matrix inversion operation and obtaining the well convergence of the calculation; (2) Based on the foraging principle of the ant colony, it can quickly compare the magnitudes of the objective function values in different intervals and determine the minimum value of the objective function, and then combine the characteristics of the system oscillation mode with the three frequency components to calculate and obtain the system oscillation mode, which makes the proposed method have well speed; (3) The main computational effort of this method lies in the calculation of the target function value and the comparison operation between different interval function values. The speed of solving the oscillation pattern can be further improved by reasonably narrowing and

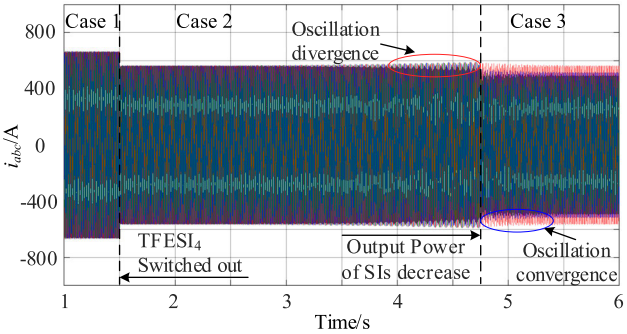

FIGURE 7. Time domain simulation waveform of system.

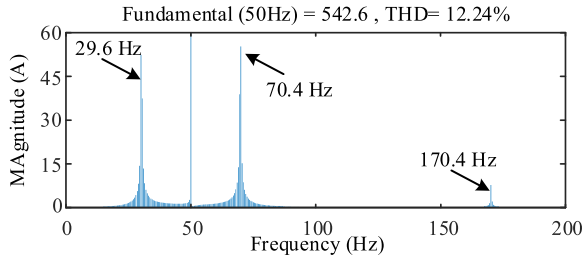

FIGURE 8. FFT analysis of i_a during 3.5s to 5.5s.

dividing the foraging interval of the ant colony, which enables the method high flexibility.

IV. STUDY OF THE OSCILLATION CHARACTERISTICS AND LAWS

In this section, the analytical method proposed in this paper is applied to the system shown in Figure 1 to investigate its oscillation characteristics and mechanisms. Without loss of generality, to facilitate analysis, the node number is chosen to n = 5. And the energy storage is located at node 4, 5. Each node is connected to 9 single-phase inverters, with 3 single-phase inverters connected to phase A, phase B, and phase C, respectively.

A. OSCILLATION CHARACTERISTICS

System parameters are listed in Appendix B. Parameter of three phase four wire energy storage inverter can be seen in Table 6. and the single-phase rooftop photovoltaic inverters are listed in Table 7. The parameters and length of the transmission line can be seen in Table 8 and Table 9.

1) SYSTEM OSCILLATION MODE

From (15) and (16), all the system oscillation modes within 0∼200Hz are obtained, which can be seen in Table 1, Table 2 and Table 3. The Table 1 lists the oscillation modes in case1 when the TFESI4 and TFESI5 are connected into the system with the three phase SIs all generating the rated power. The Table 2 shows the oscillation modes in case2 when the TFESI4 is switched out with the three phase SIs all generating the rated power. The Table 3 shows the oscillation modes system in case3 when the TFESI4 is switched out with the

TABLE 4. Oscillation Participation factors in Case 2.

Node\s_k	s_1	s_2	s_3
1	0.0746	0.075	0.0749
2	0.1288	0.1295	0.1293
3	0.2129	0.2135	0.2133
4	0.2811	0.2808	0.2808
5	0.3026	0.2912	0.2916

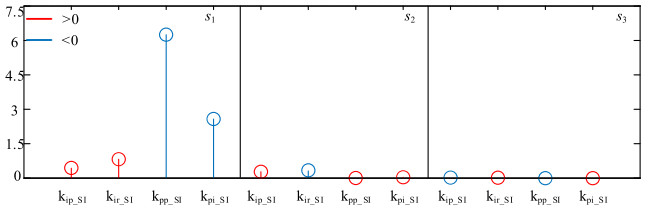

FIGURE 9. Parameter sensitivity (Y-units: −1/s).

SIs of Phase A connected to node 5 generating rated power, SIs of phase B generating half rated power and SIs of phase C generating 1/4 rated power.

From TABLE 1 and TABLE 3, the system will maintain stable in case1 and case3. From TABLE 2, in case 2, The system contains three groups of oscillation modes. Oscillation mode 1 has a positive real part and is therefore an unstable oscillation mode, indicating system instability. And oscillation mode 1 reveals that there will be oscillation components at 29.6 Hz, 70.4 Hz and 170.4Hz.

To verify the above analysis results, the model shown in Figure 1 has been established in MATLAB/Simulink. Figure 7 shows the total grid-connected currents i_{ga}, i_{gb}, i_{gc}. The system can maintain stable from 1 s to 1.5 s, while the system gradually diverges as the TFESI4 connected to node-4 removed from the system at 1.5 s. Figure 8 shows the FFT analysis of i_{ga} during divergent state of the system. From Figure 8, there are oscillation components of 29.6Hz, 70.4Hz, and 170.4Hz. The simulation results align with the oscillation modes shown in Table 2.

The system oscillation gradually converges when the generated power of SIs connected to phase B decrease to half rated power and the generated power of SIs connected to phase C decrease to 1/4 rated power, which is consistent with the oscillation modes shown in Table 3. The results that the proposed oscillation mode quantization method can accurately calculate the characteristic roots of the system and evaluate the stability under symmetric and asymmetric conditions. And the verification case of asymmetric system can be seen in section Appendix C.

2) PARTICIPATION FACTOR OF OSCILLATION MODE

The participation factors of 5 nodes for the three oscillation modes, in case 2, are obtained by combining (18), (21), and (22), and the calculating results can be seen in Table 4.

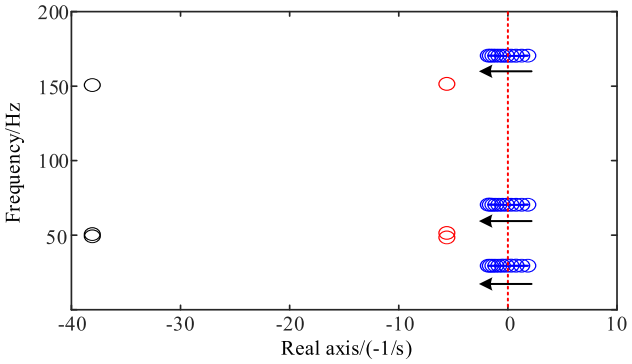

FIGURE 10. Trajectories diagram of system oscillation mode as k_{pp_SI} changes.

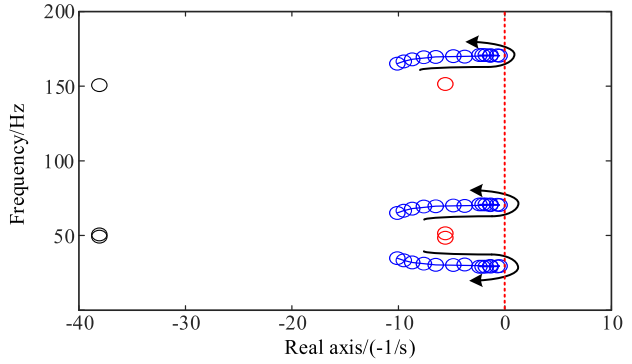

FIGURE 11. Trajectories diagram of system oscillation mode as k_{pi_SI} changes.

As can be seen from the Table 4, nodes 1 to 5 have a similar distribution of node oscillation participation factor for oscillation modes s_1, s_2 and s_3. Node 1 corresponds to the smallest influence factor and node 5 corresponds to the largest participation factor. This is because node 1 to node 5 are distributed according to a linear structure, where the short-circuit ratio of the inverter connected to node 5 is the smallest for the same transmission power. This results in node 5 contributing the most to the system oscillations.

B. STABILITY ANALYSIS OF CONTROL PARAMETERS

According to the analysis above, node 5 has the largest node oscillation participation factor, so it is important to study the influence of the control parameters of equipments connected to node 5 on the stability of the system.

The general form of sensitivity is defined as follows:

$$S(x) = \frac{\partial s_k}{\partial p}|_{p=p_0} \tag{27}$$

where, p_0 is the initial value of parameter p.

The oscillation mode sensitivities of PLL parameters (k_{pp_SI}, k_{pi_SI}) and current controller parameters (k_{ip_SI}, k_{ir_SI}) of SIs connected to node-5 are calculated according to (27) and the calculating results can be seen in Figure 9. From Figure 9, the PLL parameters k_{pp_SI} and k_{pi_SI} make a significant difference on oscillation modes 1 and no difference on mode 2 and mode 3. the current controller parameters

TABLE 5. Oscillation mode in Case4.

Oscillation mode	Band-d	Band-m	Band-u
1	1.823 +j29.78×2π	1.823 +j70.22×2π	1.823 +j170.22×2π
2	-5.62 +j48.49×2π	-5.62 +j51.51×2π	-5.62 +j151.51×2π
3	-38.09 +j49.26×2π	-38.09 +j50.74×2π	-38.09 +j150.74×2π

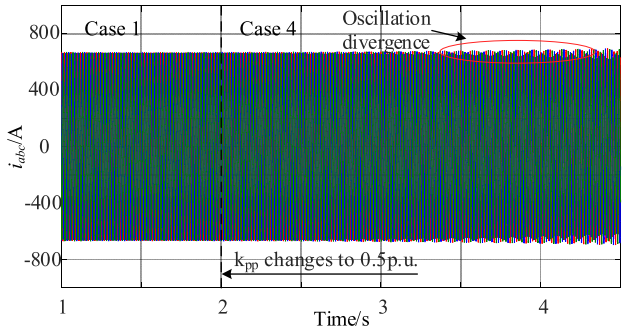

FIGURE 12. Time domain simulation waveform of system as the k_{pp} changes.

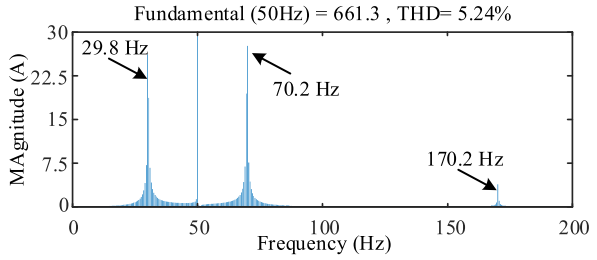

FIGURE 13. FFT analysis of i_a during 2.5s to 4.5s.

(k_{ip_SI}, k_{ir_SI}) make a significant difference on modes 1, slight difference on mode 2, and almost no difference on mode 3.

In Figure 9, it also can be observed that for oscillation mode 1, the sensitivity magnitude for k_{pp_SI} surpasses that of the other three control parameters. This suggests that variations in k_{pp_SI} have the most significant impact on this particular oscillation mode. Furthermore, it can be observed that the sensitivity magnitudes for both k_{pp_SI} and k_{pi_SI} are negative. This implies that an increase in these parameters will result in a decrease in the real part of oscillation mode 1, leading to an increase in both damping of oscillation mode 1 and the system stability margin. Conversely, the sensitivity magnitudes for k_{ip_SI} and k_{ir_SI} are positive, indicating that a reduction in these parameters will also cause a decrease in the real part of oscillation mode 1, and consequently an increase in both damping of oscillation mode 1 and the system stability margin.

To validate the results of the aforementioned analysis, k_{pp_SI}, k_{pi_SI} were selected as various control parameters. As each parameter was incrementally increased from 0.5 p.u. to 1.5 p.u., the resulting changes in the trajectories of oscillation mode were depicted in Figures 10 and 11.

Figure 10 illustrates that as k_{ip_SI} increases, oscillation mode 1 is significantly impacted while oscillation modes 2 and 3 remain largely unaffected. Oscillation mode 1 gradually shifts to the left, resulting in an increase in both damping and stability, which aligns with the findings of the sensitivity analysis. When k_{ip_SI} reaches 0.9 p.u., oscillation mode 1 enters the left half-plane and the system regains stability.

Figure 11 demonstrates that as k_{ii_SI} increases, oscillation mode 1 is significantly impacted while oscillation modes 2 and 3 remain largely unaffected. Oscillation mode 1 initially moves to the right and then to the left, causing system damping and stability to first decrease and then increase. When k_{ii_SI} reaches 0.95 p.u., oscillation mode 1 exhibits its smallest damping at -0.42, indicating that the system can maintain stability as k_{ii_SI} varies from 0.5 p.u. to 1.5 p.u..

Table 5 shows the system oscillation mode in Case 4 when the TFESI4 and TFESI5 are connected into the system with the three phase SIs all generating the rated power and k_{pp_SI5} = 0.5 p.u.

Figure 12 shows the total grid-connected currents i_{ga}, i_{gb}, i_{gc}. The system can maintain stable from 1 s to 2 s, while the system gradually diverges as the k_{pp} (proportional parameter of the SRF-PLL) of SIs connected to node-5 step from 1 p.u. to 0.8 p.u. at 2s. Figure 13 shows the FFT analysis of i_{ga} during divergent state of the system. it can be seen that there are oscillation components at 29.8Hz, 70.2Hz and 170.2Hz, which aligns with the oscillation mode 1 shown in the Table 5.

V. CONCLUSION

This paper comes up with a quantitative analysis method of oscillation mode for the multi-node three-phase four-wire system, considering the intertwined characteristic between dual frequency coupling effect and the coupling effect of sequence components. The paper can be concluded as,

(1) The 9n-dimensional NAM of the three-phase four-wire system considering DFCE and coupling effect of sequence components is constructed to encompasses the complete topology structure and all oscillation modes. Due to the consideration of DFCE and ZS components, the oscillation modes occur in group of three frequency component, with the oscillation frequencies of each component differing from each other by $2f_1$.

(2) To solve the roots of the determinant of the nodal admittance matrix efficiently, and avoiding the complicated inversion operations of the high dimensional matrix, an improved interval-based ant colony algorithm is proposed to achieve the accurate characteristic roots of the system.

(3) The node oscillation participation factor of the oscillation mode is defined to quantify the contribution of each node to the oscillation mode and locate the weaknesses of the system, which indicates that the node-5 is the weakest node in this system structure. Sensitivity can be used to investigate the degree of influence of different parameters on the oscillation mode. In case1, increasing k_{pi} or k_{pp} helps to improve the

damping of mode1 and system stability, while increasing k_{ip} or k_{ir} weakens the system stability. Additionally, the establishment of a node admittance matrix framework that considers the complete frequency coupling components and reasonable matrix reduction methods for the system are crucial aspects that will be addressed in the authors' future work.

APPENDIX

A. INFLUENCE OF THE INITIAL VOLTAGE PHASE

The related expressions of the SI can be seen as follow.

$$Y_{xref0}(s) = I_{xref0}(s)\, G_{plant}(s) \tag{A1}$$

$$Y_{xref+}(s^+) = I_{xref+}(s^+)\, G_{plant}(s^+) \tag{A2}$$

$$Y_{xref-}(s^-) = I_{xref-}(s^-)\, G_{plant}(s^-) \tag{A3}$$

$$\begin{aligned} I_{xref0}(s) = {} & 0.25 I_{ref}\left[\tilde{u}_\alpha(s) + j\tilde{u}_\beta(s)\right] G_{xpll}(s - j\omega_1) \\ & + 0.25 I_{ref}\left[\tilde{u}_\alpha(s) - j\tilde{u}_\beta(s)\right] G_{xpll}(s + j\omega) \end{aligned} \tag{A4}$$

$$\begin{aligned} I_{xref+}(s) = {} & -0.25 e^{-j2\phi_{vx}} I_{ref}\tilde{u}_\alpha(s + 2j\omega_1)\, G_{xpll}(s + j\omega_1) \\ & - 0.25 j e^{-j2\phi_{vx}} I_{ref}\tilde{u}_\beta(s + 2j\omega_1)\, G_{xpll}(s + j\omega_1) \end{aligned} \tag{A5}$$

$$\begin{aligned} I_{xref-}(s) = {} & -0.25 e^{j2\phi_{vx}} I_{ref}\tilde{u}_\alpha(s - 2j\omega_1)\, G_{xpll}(s - j\omega_1) \\ & + j0.25 e^{j2\phi_{vx}} I_{ref}\tilde{u}_\beta(s - 2j\omega_1)\, G_{xpll}(s - j\omega_1) \end{aligned} \tag{A6}$$

$$G_{xplant} = \frac{G_c G_d}{s^3 L_1 L_2 C + G_c G_d s^2 L_2 C + G_d G_c + sL_1 + sL_2} \tag{A7}$$

$$Y_{xio}(s) = \frac{1 + s^2 L_1 C + sCk_c G_d - G_f G_d}{s^3 L_1 L_2 C + k_c G_d s^2 L_2 C + G_d G_c + sL_1 + sL_2} \tag{A8}$$

$$G_{xpll}(s) = \frac{G_{xPI}(s)}{s + U_m G_{xPI}(s)} = \frac{k_{xpp} + k_{xii}/s}{s + U_m\left(k_{xpp} + k_{xii}/s\right)} \tag{A9}$$

$$\begin{aligned} \begin{bmatrix} i_{giTa}(s^-) \\ i_{giTb}(s^-) \\ i_{giTc}(s^-) \end{bmatrix} = {} & \mathbf{Y}_{re0ij}(s^-) \begin{bmatrix} u_{pccia}(s^-) \\ u_{pccib}(s^-) \\ u_{pccic}(s^-) \end{bmatrix} \\ & + \mathbf{Y}_{re+ij}(s^-) \begin{bmatrix} u_{pccia}(s) \\ u_{pccib}(s) \\ u_{pccic}(s) \end{bmatrix} \end{aligned} \tag{A10}$$

$$\begin{aligned} \mathbf{Y}_{re0ij}(s^-) = diag\Bigg(& \sum_{j=1}^{mi}\left(Y_{re0ija}(s^-)\right), \sum_{j=1}^{mi}\left(Y_{re0ijb}(s^-)\right), \\ & \times \sum_{j=1}^{mi}\left(Y_{re0ijb}(s^-)\right)\Bigg) \end{aligned} \tag{A11}$$

$$\begin{aligned} \mathbf{Y}_{re+ij}(s^-) = diag\Bigg(& \sum_{j=1}^{mi}\left(Y_{re+ija}(s^-)\right), \sum_{j=1}^{mi}\left(Y_{re+ijb}(s^-)\right), \\ & \times \sum_{j=1}^{mi}\left(Y_{re+ijc}(s^-)\right)\Bigg) \end{aligned} \tag{A12}$$

$$\begin{aligned} \begin{bmatrix} i_{giTa}(s) \\ i_{giTb}(s) \\ i_{giTc}(s) \end{bmatrix} = {} & \mathbf{Y}_{re-ij}(s) \begin{bmatrix} u_{pccia}(s^-) \\ u_{pccib}(s^-) \\ u_{pccic}(s^-) \end{bmatrix} \\ & + \mathbf{Y}_{re0ij}(s) \begin{bmatrix} u_{pccia}(s) \\ u_{pccib}(s) \\ u_{pccic}(s) \end{bmatrix} \\ & + \mathbf{Y}_{re+ij}(s) \begin{bmatrix} u_{pccia}(s^+) \\ u_{pccib}(s^+) \\ u_{pccic}(s^+) \end{bmatrix} \end{aligned} \tag{A13}$$

$$\begin{aligned} \mathbf{Y}_{re-ij}(s) = diag\Bigg(& \sum_{j=1}^{mi}\left(Y_{re-ija}(s)\right), \sum_{j=1}^{mi}\left(Y_{re-ijb}(s)\right), \\ & \times \sum_{j=1}^{mi}\left(Y_{re-ijc}(s)\right)\Bigg) \end{aligned} \tag{A14}$$

$$\begin{aligned} \mathbf{Y}_{re0ij}(s) = diag\Bigg(& \sum_{j=1}^{mi}\left(Y_{re0ija}(s)\right), \sum_{j=1}^{mi}\left(Y_{re0ijb}(s)\right), \\ & \times \sum_{j=1}^{mi}\left(Y_{re0ijc}(s)\right)\Bigg) \end{aligned} \tag{A15}$$

$$\begin{aligned} \mathbf{Y}_{re+ij}(s) = diag\Bigg(& \sum_{j=1}^{mi}\left(Y_{re+ija}(s)\right), \sum_{j=1}^{mi}\left(Y_{re+ijb}(s)\right), \\ & \times \sum_{j=1}^{mi}\left(Y_{re+ijc}(s)\right)\Bigg) \end{aligned} \tag{A16}$$

$$\begin{aligned} \begin{bmatrix} i_{giTa}(s^+) \\ i_{giTb}(s^+) \\ i_{giTc}(s^+) \end{bmatrix} = {} & \mathbf{Y}_{re-ij}(s^+) \begin{bmatrix} u_{pccia}(s) \\ u_{pccib}(s) \\ u_{pccic}(s) \end{bmatrix} \\ & + \mathbf{Y}_{re0ij}(s^+) \begin{bmatrix} u_{pccia}(s^+) \\ u_{pccib}(s^+) \\ u_{pccic}(s^+) \end{bmatrix} \end{aligned} \tag{A17}$$

$$\begin{aligned} \mathbf{Y}_{re-ij}(s^+) = diag\Bigg(& \sum_{j=1}^{m1}\left(Y_{re-ija}(s^+)\right), \sum_{j=1}^{m1}\left(Y_{re-ijb}(s^+)\right), \\ & \times \sum_{j=1}^{m1}\left(Y_{re-ijb}(s^+)\right)\Bigg) \end{aligned} \tag{A18}$$

$$\begin{aligned} \mathbf{Y}_{re0ij}(s^+) = diag\Bigg(& \sum_{j=1}^{m1}\left(Y_{re0ija}(s^+)\right), \sum_{j=1}^{m1}\left(Y_{re0ijb}(s^+)\right), \\ & \times \sum_{j=1}^{m1}\left(Y_{re0ijc}(s^+)\right)\Bigg) \end{aligned} \tag{A19}$$

The relationship between the current response at frequency s and the disturbance voltage at frequencies s^-, s, and s^+ can be obtained as shown in equations (A13).

The relationship between the current response at frequency s^+ and the disturbance voltage at frequencies s and s^+ can be

obtained as shown in equations (A17).

$$\text{Defining, } \mathbf{S}=\frac{1}{3}\begin{bmatrix}1&1&1\\1&\alpha&\alpha^2\\1&\alpha^2&\alpha\end{bmatrix},\ \mathbf{S}^{-1}=\begin{bmatrix}1&1&1\\1&\alpha^2&\alpha\\1&\alpha&\alpha^2\end{bmatrix} \tag{A20}$$

$$\begin{bmatrix}i_{giT0}(s^-)\\i_{giT1}(s^-)\\i_{giT2}(s^-)\end{bmatrix}=\mathbf{Y}^{012}_{re0i}\left(s^-\right)\begin{bmatrix}u_{pcci0}(s^-)\\u_{pcci1}(s^-)\\u_{pcci2}(s^-)\end{bmatrix}+\mathbf{Y}^{012}_{re+i}\left(s^-\right)\begin{bmatrix}u_{pcci0}(s)\\u_{pcci1}(s)\\u_{pcci2}(s)\end{bmatrix} \tag{A21}$$

In equation (22), define $\mathbf{Y}^{012}_{re0i}\left(s^-\right)=\mathbf{S}Y_{re0ij}\left(s^-\right)\mathbf{S}^{-1}$ and $\mathbf{Y}^{012}_{re+i}\left(s^-\right)=\mathbf{S}Y_{re+ij}\left(s^-\right)\mathbf{S}^{-1}$.

$$\begin{bmatrix}i_{giT0}(s)\\i_{giT0}(s)\\i_{giT0}(s)\end{bmatrix}=\mathbf{Y}^{012}_{re-i}(s)\begin{bmatrix}u_{pcci0}(s^-)\\u_{pcci1}(s^-)\\u_{pcci2}(s^-)\end{bmatrix}+\mathbf{Y}^{012}_{re0i}(s)\begin{bmatrix}u_{pcci0}(s)\\u_{pcci1}(s)\\u_{pcci2}(s)\end{bmatrix}+\mathbf{Y}^{012}_{re+i}(s)\begin{bmatrix}u_{pcci0}(s^+)\\u_{pcci1}(s^+)\\u_{pcci2}(s^+)\end{bmatrix} \tag{A22}$$

In equation (22), define the $\mathbf{Y}^{012}_{re-i}(s)=\mathbf{S}Y_{re-ij}(s)\mathbf{S}^{-1}$, $\mathbf{Y}^{012}_{re0i}(s)=\mathbf{S}Y_{re0ij}(s)\mathbf{S}^{-1}$ and $\mathbf{Y}^{012}_{re+i}(s)=\mathbf{S}Y_{re+ij}(s)\mathbf{S}^{-1}$.

$$\begin{bmatrix}i_{giT0}(s^+)\\i_{giT1}(s^+)\\i_{giT2}(s^+)\end{bmatrix}=\mathbf{Y}^{012}_{re-i}\left(s^+\right)\begin{bmatrix}u_{pcci0}(s)\\u_{pcci1}(s)\\u_{pcci2}(s)\end{bmatrix}+\mathbf{Y}^{012}_{re0i}\left(s^+\right)\begin{bmatrix}u_{pcci0}(s^+)\\u_{pcci1}(s^+)\\u_{pcci2}(s^+)\end{bmatrix} \tag{A23}$$

Inequation (23), define the $\mathbf{Y}^{012}_{re-i}\left(s^+\right)=\mathbf{S}Y_{re-ij}\left(s^+\right)\mathbf{S}^{-1}$ and $\mathbf{Y}^{012}_{re0i}\left(s^+\right)=\mathbf{S}Y_{re0ij}\left(s^+\right)\mathbf{S}^{-1}$.

B. PARAMETERS OF THE INVESTIGATED SYSTEM

See Tables 6–9.

C. VERIFICATION CASE OF ASYMMETRIC SYSTEM

The node of the verification case of studied asymmetrical system is also five. And the energy storage inverters are located at node 4, 5. Node 1 and node 3 are each connected to three single-phase inverters for phases A, B, and C. Node 5 is connected to six inverters for phases A, B, and C. Node 2 is only connected to three single-phase inverters for phase C, while node 4 is only connected to three single-phase inverters for phase B.

The Table 10 lists the oscillation modes in case5 when the three phase SIs all generating the rated power and $k_{pp}=1$ p.u.. The Table 11 shows the oscillation modes in case6 when the three phase SIs all generating the rated power and $k_{pp}=0.55$ p.u.. The Table 12 shows the oscillation modes in case7 when the SIs of Phase A connected to node 5 generating rated power, SIs of phase C generating half rated power and SIs of phase B generating 1/4 rated power.

TABLE 6. Parameter of TFESIs.

Symbol	Parameter	Value
U_{sTF}	Rated voltage	380 V
P_{sTF}	Rated power	50kW
f_1	Fundamental frequency	50 Hz
f_{sTF}	Switching frequency	10 kHz
V_{dcTF}	Dc-link voltage	700 V
L_f	Filter inductance	3 mH
R_{Lf}	parasitic resistance of filter inductance	0.1Ω
k_{ppTF}	Proportional gain of PLL controller	0.0158
k_{piTF}	Integral gain of PLL controller	0.9920
k_{dip}	Proportional gain of d-axis current controller	1.6
k_{dii}	Integral gain of d-axis current controller	120.7
k_{qip}	Proportional gain of q-axis current controller	1.6
k_{qii}	Integral gain of q-axis current controller	120.7
k_{0ip}	Proportional gain of zero-axis current controller	3
k_{0ir}	Resonant gain of zero-axis current controller	120

TABLE 7. Parameter of SIs.

Symbol	Parameter	Value
U_{sSI}	Rated voltage	380 V
P_{sSI}	Rated power	5 kW
f_{1SI}	Fundamental frequency	50 Hz
f_{sSI}	Switching frequency	15 kHz
V_{dcSI}	Dc-link voltage	700 V
L_1	Filter inductance	0.75 mH
R_1	parasitic resistance of filter inductance	0.1Ω
L_2	Filter inductance	0.45 mH
R_2	parasitic resistance of filter inductance	0.1Ω
C	Filter capacitor	6.8 μF
R_3	parasitic resistance of filter capacitor	0.1Ω
k_{ipSI}	Proportional gain of PR current controller	9
k_{irSI}	Resonant gain of PR current controller	600
G_f	PCC voltage feed forward control coefficient	0.6
k_c	Active damping coefficient	6
k_{ppSI}	Proportional gain of PLL controller	0.09
k_{piSI}	Integral gain of PLL controller	60

TABLE 8. Parameter of transmission line.

Voltage rate/kV	Resistance/(Ω/km)	Inductance/(mH/km)
380	0.13	0.24

TABLE 9. Length of transmission line.

Line number	Length of transmission line (m)
L_{12}	200
L_{23}	300
L_{34}	300
L_{45}	200

TABLE 10. Oscillation modes in Case5.

Oscillation mode	Band-d	Band-m	Band-u
1	-3.10 +j29.70×2π	-3.10 +j70.30×2π	-3.10 +j170.30×2π
2	-5.62 +j48.49×2π	-5.62 +j51.51×2π	-5.62 +j151.51×2π
3	-38.09 +j49.26×2π	-38.09 +j50.74×2π	-38.09 +j150.74×2π

TABLE 11. Oscillation modes in Case6.

Oscillation mode	Band-d	Band-m	Band-u
1	1.20 +j30.50×2π	1.20 +j69.50×2π	1.20 +j169.50×2π
2	-5.60 +j48.50×2π	-5.60 +j51.50×2π	-5.60 +j151.50×2π
3	-38.20 +j49.30×2π	-38.20 +j50.70×2π	-38.20 +j150.70×2π

TABLE 12. Oscillation modes in Case7.

Oscillation mode	Band-d	Band-m	Band-u
1	-0.91 +j30.70×2π	-0.91 +j69.30×2π	-0.91 +j169.30×2π
2	-5.61 +j48.49×2π	-5.61 +j51.51×2π	-5.61 +j151.51×2π
3	-38.20 +j49.30×2π	-38.20 +j50.70×2π	-38.20 +j150.70×2π

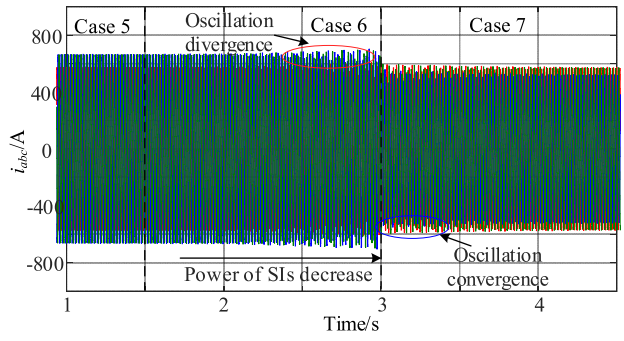

FIGURE 14. Time domain simulation waveform of the asymmetric system.

Figure 14 shows the total grid-connected currents i_{ga}, i_{gb}, i_{gc}. The system can maintain stable from 1 s to 1.5 s, while the system gradually diverges as the k_{pp} (proportional parameter of the SRF-PLL) of SIs connected to node-5 step from 1 p.u. to 0.55 p.u. at 1.5s. Figure 15 shows the FFT analysis of i_{ga} during divergent state of the system. There are oscillation components at 30.5Hz, 69.5Hz and 169.5Hz, which aligns with the oscillation mode 1 shown in the Table 11.

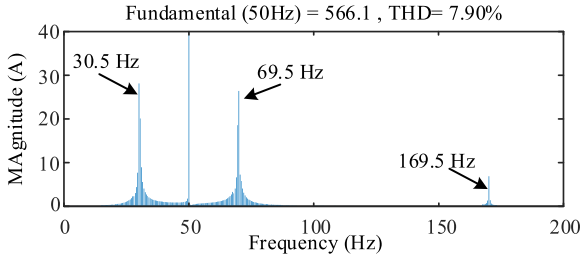

FIGURE 15. FFT analysis of i_a during 1.5s to 3.5s.

The system oscillation gradually converges when the generated power of SIs connected to phase C decrease to half rated power and the generated power of SIs connected to phase B decrease to 1/4 rated power, which is consistent with the oscillation modes shown in TABLE 12.

REFERENCES

[1] A. R. Malekpour, A. Pahwa, and B. Natarajan, "Hierarchical architecture for integration of rooftop PV in smart distribution systems," *IEEE Trans. Smart Grid*, vol. 9, no. 3, pp. 2019–2029, May 2018.
[2] S. A. E. Batawy and W. G. Morsi, "Optimal secondary distribution system design considering rooftop solar photovoltaics," *IEEE Trans. Sustain. Energy*, vol. 7, no. 4, pp. 1662–1671, Oct. 2016.
[3] A. M. M. Nour, A. Y. Hatata, A. A. Helal, and M. M. El-Saadawi, "Review on voltage-violation mitigation techniques of distribution networks with distributed rooftop PV systems," *IET Gener., Transmiss. Distrib.*, vol. 14, no. 3, pp. 349–361, Feb. 2020.
[4] M. Zeraati, M. E. H. Golshan, and J. M. Guerrero, "Voltage quality improvement in low voltage distribution networks using reactive power capability of single-phase PV inverters," *IEEE Trans. Smart Grid*, vol. 10, no. 5, pp. 5057–5065, Sep. 2019.
[5] Q. Chai, C. Zhang, Y. Xu, and Z. Y. Dong, "PV inverter reliability-constrained volt/var control of distribution networks," *IEEE Trans. Sustain. Energy*, vol. 12, no. 3, pp. 1788–1800, Jul. 2021.
[6] A. Mokaribolhassan, G. Nourbakhsh, G. Ledwich, A. Arefi, and M. Shafiei, "Distribution system state estimation using PV separation strategy in LV feeders with high levels of unmonitored PV generation," *IEEE Syst. J.*, vol. 17, no. 1, pp. 684–695, Mar. 2023.
[7] A. Zahedmanesh, K. M. Muttaqi, and D. Sutanto, "An adaptable correlated control for maintaining voltage quality in low-voltage distribution grids containing PVs and PEVs," *IEEE Trans. Ind. Informat.*, vol. 18, no. 9, pp. 5804–5814, Sep. 2022.
[8] M. Zeraati, M. E. H. Golshan, and J. M. Guerrero, "Distributed control of battery energy storage systems for voltage regulation in distribution networks with high PV penetration," *IEEE Trans. Smart Grid*, vol. 9, no. 4, pp. 3582–3593, Jul. 2018.
[9] Y. Ren, X. Wang, L. Chen, Y. Min, G. Li, L. Wang, and Y. Zhang, "A strictly sufficient stability criterion for grid-connected converters based on impedance models and Gershgorin's theorem," *IEEE Trans. Power Del.*, vol. 35, no. 3, pp. 1606–1609, Jun. 2020.
[10] C. Li, "Unstable operation of photovoltaic inverter from field experiences," *IEEE Trans. Power Del.*, vol. 33, no. 2, pp. 1013–1015, Apr. 2018.
[11] S. Behzadirafi and F. de León, "Closed-form determination of the impedance locus plot of fault current limiters: A rigorous approach with graphical representation," *IEEE Trans. Power Del.*, vol. 33, no. 6, pp. 2710–2717, Dec. 2018.
[12] R. S. R. Sankar, S. V. J. Kumar, and G. M. Rao, "Impedance based stability analysis of single-phase PV inverter connected to weak grid with voltage feed forward control," in *Proc. IEEE Int. Conf. Power, Control, Signals Instrum. Eng. (ICPCSI)*, Sep. 2017, pp. 2187–2194.

[13] L. Harnefors, X. Wang, A. G. Yepes, and F. Blaabjerg, "Passivity-based stability assessment of grid-connected VSCs—An overview," *IEEE J. Emerg. Sel. Topics Power Electron.*, vol. 4, no. 1, pp. 116–125, Mar. 2016.

[14] B. Wen, D. Boroyevich, R. Burgos, P. Mattavelli, and Z. Shen, "Analysis of D-Q small-signal impedance of grid-tied inverters," *IEEE Trans. Power Electron.*, vol. 31, no. 1, pp. 675–687, Jan. 2016.

[15] B. Wen, D. Dong, D. Boroyevich, R. Burgos, P. Mattavelli, and Z. Shen, "Impedance-based analysis of grid-synchronization stability for three-phase paralleled converters," *IEEE Trans. Power Electron.*, vol. 31, no. 1, pp. 26–38, Jan. 2016.

[16] B. Hu, H. Nian, M. Li, Y. Liao, J. Yang, and H. Tong, "Impedance characteristic analysis and stability improvement method for DFIG system within PLL bandwidth based on different reference frames," *IEEE Trans. Ind. Electron.*, vol. 70, no. 1, pp. 532–543, Jan. 2023.

[17] C. Zhang, M. Molinas, S. Føyen, J. A. Suul, and T. Isobe, "Harmonic-domain SISO equivalent impedance modeling and stability analysis of a single-phase grid-connected VSC," *IEEE Trans. Power Electron.*, vol. 35, no. 9, pp. 9770–9783, Sep. 2020.

[18] Q. Qian, S. Xie, J. Xu, K. Xu, S. Bian, and N. Zhong, "Output impedance modeling of single-phase grid-tied inverters with capturing the frequency-coupling effect of PLL," *IEEE Trans. Power Electron.*, vol. 35, no. 5, pp. 5479–5495, May 2020.

[19] J. Xu, H. Qian, S. Bian, Y. Hu, and S. Xie, "Comparative study of singlephase phase-locked loops for grid-connected inverters under non-ideal grid conditions," *CSEE J. Power Energy Syst.*, vol. 8, no. 1, pp. 155–164, Jan. 2022.

[20] J. Xu, S. Bian, Q. Qian, H. Qian, and S. Xie, "Robustness improvement of single-phase inverters under weak grid cases by adding grid current feedforward in delay-based phase-locked loop," *IEEE Access*, vol. 8, pp. 124275–124287, 2020.

[21] J. Xu, H. Qian, Q. Qian, and S. Xie, "Modeling, stability, and design of the single-phase SOGI-based phase-locked loop considering the frequency feedback loop effect," *IEEE Trans. Power Electron.*, vol. 38, no. 1, pp. 987–1002, Jan. 2023.

[22] H. Nian, Y. Liao, M. Li, D. Sun, Y. Xu, and B. Hu, "Impedance modeling and stability analysis of three-phase four-leg grid-connected inverter considering zero-sequence," *IEEE Access*, vol. 9, pp. 83676–83687, 2021.

[23] G. Feng, Z. Ye, Y. Xia, L. Huang, and Z. Wang, "Impedance modeling and stability analysis of three-phase four-wire inverter with grid-connected operation," *Energies*, vol. 15, no. 8, p. 2754, Apr. 2022.

[24] J. He, Y. W. Li, D. Bosnjak, and B. Harris, "Investigation and active damping of multiple resonances in a parallel-inverter-based microgrid," *IEEE Trans. Power Electron.*, vol. 28, no. 1, pp. 234–246, Jan. 2013.

[25] Y. Wang, X. Wang, F. Blaabjerg, and Z. Chen, "Harmonic instability assessment using state-space modeling and participation analysis in inverter-fed power systems," *IEEE Trans. Ind. Electron.*, vol. 64, no. 1, pp. 806–816, Jan. 2017.

[26] Z. Shuai, Y. Peng, X. Liu, Z. Li, J. M. Guerrero, and Z. J. Shen, "Parameter stability region analysis of islanded microgrid based on bifurcation theory," *IEEE Trans. Smart Grid*, vol. 10, no. 6, pp. 6580–6591, Nov. 2019.

[27] C. Yoon, X. Wang, C. L. Bak, and F. Blaabjerg, "Stabilization of multiple unstable modes for small-scale inverter-based power systems with impedance-based stability analysis," in *Proc. IEEE Appl. Power Electron. Conf. Expo. (APEC)*, Charlotte, NC, USA, Mar. 2015, pp. 1202–1208.

[28] W. Xu, Z. Huang, Y. Cui, and H. Wang, "Harmonic resonance mode analysis," *IEEE Trans. Power Del.*, vol. 20, no. 2, pp. 1182–1190, Apr. 2005.

[29] C. Yoon, H. Bai, R. N. Beres, X. Wang, C. L. Bak, and F. Blaabjerg, "Harmonic stability assessment for multiparalleled, grid-connected inverters," *IEEE Trans. Sustain. Energy*, vol. 7, no. 4, pp. 1388–1397, Oct. 2016.

[30] X. Wang, F. Blaabjerg, and P. C. Loh, "An impedance-based stability analysis method for paralleled voltage source converters," in *Proc. Int. Power Electron. Conf.*, Hiroshima, Japan, May 2014, pp. 1529–1535.

[31] E. Ebrahimzadeh, F. Blaabjerg, X. Wang, and C. L. Bak, "Harmonic stability and resonance analysis in large PMSG-based wind power plants," *IEEE Trans. Sustain. Energy*, vol. 9, no. 1, pp. 12–23, Jan. 2018.

[32] Y. Zhan, X. Xie, and Y. Wang, "Impedance network model based modal observability and controllability analysis for renewable integrated power systems," *IEEE Trans. Power Del.*, vol. 36, no. 4, pp. 2025–2034, Aug. 2021.

[33] Y. Li, Z. Shuai, X. Liu, Y. Chen, Z. Li, Y. Hong, and Z. J. Shen, "Stability analysis and location optimization method for multiconverter power systems based on nodal admittance matrix," *IEEE J. Emerg. Sel. Topics Power Electron.*, vol. 9, no. 1, pp. 529–538, Feb. 2021.

[34] Z. Tang, D. J. Hill, and T. Liu, "Distributed coordinated reactive power control for voltage regulation in distribution networks," *IEEE Trans. Smart Grid*, vol. 12, no. 1, pp. 312–323, Jan. 2021.

[35] W. Jiao, J. Chen, Q. Wu, C. Li, B. Zhou, and S. Huang, "Distributed coordinated voltage control for distribution networks with DG and OLTC based on MPC and gradient projection," *IEEE Trans. Power Sys.*, vol. 37, no. 1, pp. 680–690, Jan. 2022.

[36] Y. Yu, G.-P. Liu, and W. Hu, "Coordinated distributed predictive control for voltage regulation of DC microgrids with communication delays and data loss," *IEEE Trans. Smart Grid*, vol. 14, no. 3, pp. 1708–1722, May 2023.

[37] L. Lin, Q. Jia, C. Lv, J. Liang, and P. Luo, "Partitional collaborative mitigation strategy of distribution network harmonics based on distributed model predictive control," *IEEE Trans. Smart Grid*, vol. 14, no. 3, pp. 1998–2009, May 2023.

[38] E. Ebrahimzadeh, F. Blaabjerg, X. Wang, and C. L. Bak, "Bus participation factor analysis for harmonic instability in power electronics based power systems," *IEEE Trans. Power Electron.*, vol. 33, no. 12, pp. 10341–10351, Dec. 2018.

[39] M. K. Bakhshizadeh, X. Wang, F. Blaabjerg, J. Hjerrild, L. Kocewiak, C. L. Bak, and B. Hesselbæk, "Couplings in phase domain impedance modeling of grid-connected converters," *IEEE Trans. Power Electron.*, vol. 31, no. 10, pp. 6792–6796, Oct. 2016.

[40] W. Cao, Y. Ma, and F. Wang, "Sequence-impedance-based harmonic stability analysis and controller parameter design of three-phase inverter-based multibus AC power systems," *IEEE Trans. Power Electron.*, vol. 32, no. 10, pp. 7674–7693, Oct. 2017.

[41] X. Wang, F. Blaabjerg, and P. C. Loh, "Virtual *RC* damping of *LCL*-filtered voltage source converters with extended selective harmonic compensation," *IEEE Trans. Power Electron.*, vol. 30, no. 9, pp. 4726–4737, Sep. 2015.

[42] Q. Qian, S. Xie, L. Huang, J. Xu, Z. Zhang, and B. Zhang, "Harmonic suppression and stability enhancement for parallel multiple grid-connected inverters based on passive inverter output impedance," *IEEE Trans. Ind. Electron.*, vol. 64, no. 9, pp. 7587–7598, Sep. 2017.

[43] A. Sangwongwanich, Y. Yang, D. Sera, H. Soltani, and F. Blaabjerg, "Analysis and modeling of interharmonics from grid-connected photovoltaic systems," *IEEE Trans. Power Electron.*, vol. 33, no. 10, pp. 8353–8364, Oct. 2018.

[44] X. Li, Z. Deng, Z. Chen, and Q. Fei, "Analysis and simplification of three-dimensional space vector PWM for three-phase four-leg inverters," *IEEE Trans. Ind. Electron.*, vol. 58, no. 2, pp. 450–464, Feb. 2011.

[45] J. J. Grainger and W. D. Stevenson, *Power System Analysis*. New York, NY, USA: McGraw-Hill, 1994.

[46] H. Liu, X. Xie, X. Gao, H. Liu, and Y. Li, "Stability analysis of SSR in multiple wind farms connected to series-compensated systems using impedance network model," *IEEE Trans. Power Syst.*, vol. 33, no. 3, pp. 3118–3128, May 2018.

[47] G. Strang, *Introduction to Linear Algebra*. 5th ed. London, U.K.: Wellesley-Cambridge Press, 2016.

[48] H. Zong, C. Zhang, J. Lyu, X. Cai, and M. Molinas, "Block diagonal dominance-based model reduction method applied to MMC asymmetric stability analysis," *IEEE Trans. Energy Convers.*, vol. 36, no. 3, pp. 2438–2451, Sep. 2021.

YUMING LIAO was born in Ganzhou, Jiangxi, China. He received the M.Eng. degree in electronics and power transmission from the Department of Electrical Engineering, Hefei University of Technology, Hefei, China, in 2018. He is currently pursuing the Ph.D. degree in electrical engineering with Zhejiang University, Hangzhou, China.

His research interests include stability analysis of grid-connected operation control and renewable source generation system stability.

YAOXIN WANG (Student Member, IEEE) was born in Changzhi, China. He received the B.Eng. degree in electrical engineering from Zhejiang University, Hangzhou, China, in 2021, where he is currently pursuing the M.Eng. degree in electrical engineering.

His research interests include the dc-impedance-based stability analysis methods for VSCs-based power systems under weak grids and the corresponding impedance reshaping control strategy.

HENG NIAN (Senior Member, IEEE) received the B.Eng. and M.Eng. degrees in electrical engineering from the Hefei University of Technology, China, in 1999 and 2002, respectively, and the Ph.D. degree in electrical engineering from Zhejiang University, China, in 2005.

From 2005 to 2007, he was a Postdoctoral Researcher with the College of Electrical Engineering, Zhejiang University. In 2007, he was promoted to Associate Professor. From 2013 to 2014, he was a Visiting Scholar with the Department of Electrical, Computer, and Systems Engineering, Rensselaer Polytechnic Institute, Troy, NY, USA. Since 2016, he has been a Full Professor with the College of Electrical Engineering, Zhejiang University. He has published more than 40 IEEE/IET TRANSACTIONS papers and holds more than 20 issued/pending patents. His current research interests include the optimal design and operation control for wind power generation systems.

HAIPAN LI was born in Shanxi, China. He received the B.Eng. degree from Zhejiang University, Hangzhou, China, in 2020, where he is currently pursuing the Ph.D. degree in electrical engineering.

His research interests include small-signal modeling of renewable generators and their integration to the electric grid and system stability analysis.

YUKUN QIU was born in Ruian, China. He received the B.Eng. degree in electrical engineering from Zhejiang University, Hangzhou, China, in 2022, where he is currently pursuing the M.Eng. degree in electrical engineering.

His research interest includes the optimization of renewable energy grid connections.

DAN SUN (Senior Member, IEEE) received the B.S. degree in electrical engineering from Shenyang Jianzhu University, Shenyang, China, in 1997, the M.S. degree in electrical engineering from Hohai University, Nanjing, China, in 2000, and the Ph.D. degree in electrical engineering from Zhejiang University, Hangzhou, China, in 2004.

In 2004, she joined the College of Electrical Engineering, Zhejiang University. Since 2017, she has been a Full Professor with Zhejiang University. Her research interests include advanced electric machine drives and control for wind power generation systems.